COBEM 2023 27TH INTERNATIONAL CONGRESS OF MECHANICAL ENGENEERING

ABCM Brazilian Society of Mechanical Sciences and Engineering
27th ABCM International Congress of Mechanical Engineering
December 04-08, 2023, Florianópolis-SC, Brazil

COB-2023-0054
STUDY OF A NONLINEAR AEROELASTIC MODEL WITH COMBINED SMA-BASED STRUCTURAL HYSTERESIS AND DYNAMIC STALL

Lucas Victorelli Caravita
Luís Felipe Moreira da Silva Cassales
Multicampus Electrical Engineering Graduate Program, Science and Technology Institute of Sorocaba (ICTS) and School of Engineering of Sao Joao da Boa Vista (FESJ), Sao Paulo State University (Unesp). Av. Profª. Isette Corrêa Fontão 505, São João da Boa Vista, SP, Brazil, 13876-750.
lucas.caravita@unesp.br
luis.cassales@unesp.br

Giovanne Sooma Assuncao Silva
Vagner Candido de Sousa
Department of Aeronautical Engineering, School of Engineering of Sao Joao da Boa Vista (FESJ), Sao Paulo State University (Unesp). Av. Profª. Isette Corrêa Fontão 505, São João da Boa Vista, SP, Brazil, 13876-750.
giovanne.sooma@unesp.br
vagner.sousa@unesp.br

Abstract. *This study focuses on the aeroelastic behavior of a pitch-and-plunge airfoil undergoing nonlinear oscillations related to shape-memory alloy hysteresis and dynamic stall. The shape-memory alloy behavior is modeled based on the well-known Brinson's model. The unsteady aerodynamic loading is represented by the nonlinear Beddoes-Leishman model. Numerical results are comparable when linear (oversimplified by neglecting nonlinear contributions) and nonlinear (complete model) aerodynamic representations are considered in cases specifically at the flutter boundary of the airfoil and for relatively small initial disturbances. With increasing airflow speeds the amplitudes of oscillation grow over time and the linear aerodynamic model overestimates the amplitudes more severely. For the same conditions, the nonlinear model predicts the transformation of unstable oscillations into limit-cycles of smaller amplitudes (in agreement with experimental data from the literature). The presence of the shape-memory material is qualitatively similar in effect, but structurally introduced via hysteretic damping of reversible austenitic-martensitic phase transformation. The results also depict the attractiveness of combined structural and aerodynamic nonlinearities to airfoil-based energy harvesting purposes, predicting bounded oscillations at higher post-flutter airflow speeds when compared with cases for isolated structural or aerodynamic nonlinear behaviors. Although no attention is pay to the quantitative amount of electrical power obtained (not included in the scope of this study), the predicted operating envelope of the combined nonlinear effects considered here seems superior to that obtained from other previously investigated strategies.*

Keywords: *nonlinear aeroelasticity, Beddoes-Leishman, dynamic stall, shape-memory alloys, smart structures*

1. INTRODUCTION

Aeroelastic phenomena have been studied within several fields of engineering, including aeronautical and aerospace, civil, ocean and oil, and wind turbine fields. The classical linear flutter, characterized by dynamically unstable structural behavior of an aerodynamic surface, is widely investigated (Bisplinghoff *et al.*, 1955; Dowell, 2015). In the past few decades, nonlinear phenomena have also been considered, to capture the aeroelastic behavior of bodies in the presence of structural and aerodynamic nonlinearities. Structural nonlinearity sources are typically related to damping and stiffness (*e.g.*, freeplay, hardening and softening polynomial and asymmetric restoring loading, and hysteresis), while aerodynamic nonlinearity sources are typically related to shock waves (at relatively high Mach numbers), tip vortices, and flow-separation stall in rotary wing and blade problems (Lee *et al.*, 1999). More recently, dynamic stall-related phenomena have been appreciated also in airfoil-based energy harvesting studies (Santos *et al.*, 2019).

This study focus on the aeroelastic behavior of a classical airfoil section undergoing self-sustained nonlinear oscillations related to structural nonlinearities of hysteretic type due to elements with shape-memory effects and aerodynamic nonlinearities due to the dynamic stall phenomenon when pitching at large amplitudes. The airfoil is modeled as a classical rigid-body two-degree-of-freedom (2-DoF) pitch-and-plunge-airfoil (PAPA) model based on lumped spring-mass assumption, where the coupled aeroelastic displacements are achieved by a combination of translational and torsional springs. The translational spring is assumed linearly elastic while the torsional spring introduces the pseudoelastic (and hysteretic) behavior of typical shape-memory alloy (SMA) elements mechanically loaded and unloaded at temperatures

above their austenite finish temperatures.

The aeroelastic model with SMA springs is based on Sousa and De Marqui Junior (2016) and Sousa and De Marqui (2018). The shape-memory alloy behavior is modeled based on the well-known Brinson's model (Brinson, 1993), with a few improvements such as radial distribution of state variables (including a representation of nonhomogeneous and nonlinear cross-sectional distributions of shear stress and martensite volume fraction) (Sousa *et al.*, 2017). The referred articles discuss (numerically and experimentally) the main effects of stress-induced SMA phase transformation on the aeroelastic behavior of an airfoil model similar to that considered here, where it is shown the SMA springs need to be preloaded in order to achieve the hysteresis loop (hysteretic damping) as the airfoil oscillates at or above its critical flutter speed. A pertinent aspect concerning with the preload level is that it should be carefully appreciated according with the model characteristics in the sense that too few preload will fail in transforming unstable oscillations into stable oscillations before the amplitudes reach unacceptably large values, and that too much preload will impede the recovery of the austenitic phase during the unloading stage of the SMA springs so that the hysteretic behavior is replaced by linear behavior with an offset in the stress-strain plane and no energy dissipation effect is achieved.

The unsteady aerodynamic loading is represented by the nonlinear Beddoes-Leishman model (Beddoes, 1978; Leishman and Beddoes, 1986, 1989; Leishman and Crouse, 1989a,b), and is (qualitatively and quantitatively) verified with more recent works from the literature (Vasconcellos *et al.*, 2016; Santos *et al.*, 2017, 2019). In addition to the investigation of the general aeroelastic behavior of the airfoil under consideration when oscillating at relatively large amplitudes, this study also has the secondary objective of evaluating the attractiveness of combined structural and aerodynamic nonlinearity sources to airfoil-based energy harvesting purposes with respect to other strategies presented in the literature. In cases where the airfoil is considered for energy harvesting purposes (with electromechanical coupling) the pseudoelastic behavior is assumed to take place at temperatures below room temperature so that no extra heat sources would be required for thermal activation of the SMA springs (Sousa and De Marqui Junior, 2015; Sousa and De Marqui, 2018).

Numerical results are comparable when linear (oversimplified by neglecting nonlinear contributions) and nonlinear (complete model) aerodynamic representations are considered in cases specifically at the flutter boundary of the airfoil and for relatively small initial disturbances. With increasing airflow speeds the amplitudes of oscillation grow over time and the linear aerodynamic model overestimates the amplitudes more severely. For the same conditions, the nonlinear model predicts the transformation of unstable oscillations into limit-cycles of smaller amplitudes (in agreement with experimental data from the literature). The presence of the shape-memory material is qualitatively similar in effect, but structurally introduced via hysteretic damping of reversible austenitic-martensitic (pseudoelastic) SMA phase transformation. The results also depict the attractiveness of combined structural and aerodynamic nonlinearities to airfoil-based energy harvesting purposes since wider ranges of airflow speeds with stable post-flutter oscillations are expected.

2. MATHEMATICAL MODEL

In this section, the equations of motion of an airfoil model, as depicted in Fig. 1, are coupled with the nonlinear Beddoes-Leishman unsteady aerodynamic model. The torsional stiffness of the airfoil accounts for stress-induced SMA pseudoelastic hysteresis. The structural displacements are denoted by h for the linear plunge motion and θ for the angular pitch motion (positive as indicated in the figure). The span-normalized aeroelastic parameters are the airfoil mass (m_θ and m_h for the rotational and translational motions), moment of inertia about the elastic center (I_θ), linear plunge stiffness (k_h), torsional pitch stiffness (k_θ), and modal damping ratios (ζ_h and ζ_θ). The airfoil characteristic lengths and locations are the span length (l), chord length (c), semichord length ($b = c/2$), center of gravity (CG), elastic center (e.c., x_{ec}), normalized CG–x_{ec} offset (x_θ), and aerodynamic center (a.c., x_{ac}). The unsteady aerodynamic loading (per unit of span length) is represented by lifting force (L) and pitching moment (M_θ).

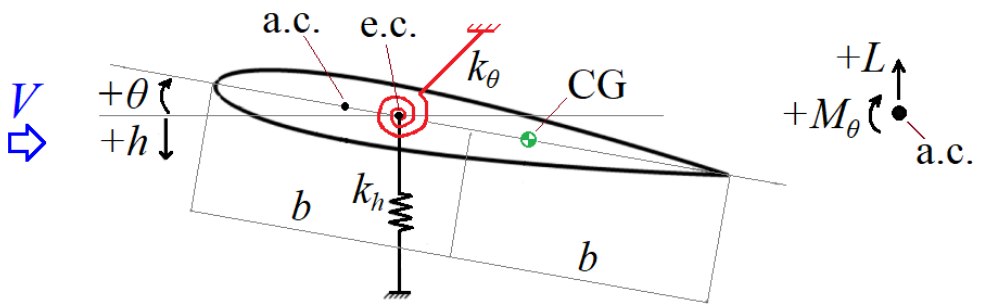

Figure 1. Pitch-and-plunge-airfoil (PAPA) model (damping representation omitted for clarity).

2.1 Beddoes-Leishman Aerodynamic Model

The Beddoes-Leishman unsteady aerodynamic model to represent the aeroelastic behavior of an airfoil section undergoing either linear (small-amplitude) flutter oscillations or nonlinear (large-amplitude) stall-related oscillations is described based on Beddoes (1978), Leishman and Beddoes (1986, 1989), Leishman and Crouse (1989a,b), and Santos *et al.* (2017, 2019), represented in state-space form, with eight state variables associated with the linear contribution to the aerodynamic loading and four state variables associated with the nonlinear contribution,

$$\dot{\mathbf{x}} = \mathbf{A}\mathbf{x} + \mathbf{B}\left\{ \begin{array}{c} \alpha \\ q \end{array} \right\}, \tag{1}$$

where the overdot denotes time derivative, $\mathbf{x}$ is the vector of linear aerodynamic state variables, $(x_1,\ \ldots,\ x_8)$, $\mathbf{A}$ is a diagonal matrix with constant elements defined as $a_{11} = -b_1\beta^2 V/b$, $a_{22} = -b_2\beta^2 V/b$, $a_{33} = -1/(K_\alpha T_I)$, $a_{44} = -1/(K_q T_I)$, $a_{55} = -1/(b_3 K_{\alpha M} T_I)$, $a_{66} = -1/(b_4 K_{\alpha M} T_I)$, $a_{77} = -b_5\beta^2 V/b$, and $a_{88} = -1/(K_{qM} T_I)$, with $\beta = \sqrt{1-M^2}$ (compressibility factor), $M = V/V_s$ (Mach Number), V is the airflow speed, V_s is the speed of sound, $T_I = c/V_s$,

$$\begin{array}{l} K_\alpha = 0.75\big/\big[(1-M) + \pi\beta^2 M^2\,(A_1 b_1 + A_2 b_2)\big] \\ K_q = 0.75\big/\big[(1-M) + 2\pi\beta^2 M^2\,(A_1 b_1 + A_2 b_2)\big] \\ K_{\alpha M} = (A_3 b_4 + A_4 b_3)/[b_3 b_4\,(1-M)] \\ K_{qM} = 7\big/\big[15\,(1-M) + 3\pi\beta M^2 b_5\big] \end{array}, \tag{2}$$

$A_1 = 0.3$, $A_2 = 0.7$, $A_3 = 1.5$, $A_4 = -0.5$, $A_5 = 1.0$, $b_1 = 0.14$, $b_2 = 0.53$, $b_3 = 0.25$, $b_4 = 0.1$, and $b_5 = 0.5$ are constant model parameters, $\mathbf{B}$ is composed of constant values,

$$\mathbf{B} = \begin{bmatrix} 1 & 1 & 1 & 0 & 1 & 1 & 0 & 0 \\ 0.5 & 0.5 & 0 & 1 & 0 & 0 & 1 & 1 \end{bmatrix}^T, \tag{3}$$

$\alpha = \theta + \arctan(\dot{h}/V)$ is the aerodynamic angle of attack, and $q = c\dot{\theta}/V$ is the dimensionless pitch rate.

The following output equation provides the linear contributions to the total aerodynamic loading coefficients,

$$\left\{ \begin{array}{c} C_n^p \\ C_m^p \end{array} \right\} = \mathbf{C}\mathbf{x} + \mathbf{D}\left\{ \begin{array}{c} \alpha \\ q \end{array} \right\}, \tag{4}$$

where C_n^p is the (linear) normal force coefficient and C_m^p is the (linear) pitching moment coefficient, which are needed in the nonlinear aerodynamic equations. Matrices $\mathbf{C}$ and $\mathbf{D}$ are defined,

$$\mathbf{C} = \begin{bmatrix} c_{11} & c_{12} & c_{13} & c_{14} & 0 & 0 & 0 & 0 \\ c_{21} & c_{22} & 0 & 0 & c_{25} & c_{26} & c_{27} & c_{28} \end{bmatrix}, \tag{5}$$

$$\mathbf{D} = \left[\begin{array}{cc} \frac{4}{M} & \frac{1}{M} \\ -\frac{1}{M} & -\frac{7}{12M} \end{array} \right], \tag{6}$$

where $c_{11} = C_{n\alpha}\beta^2 A_1 b_1 V/b$, $c_{12} = C_{n\alpha}\beta^2 A_2 b_2 V/b$, $c_{13} = -4/(MK_\alpha T_I)$, $c_{14} = -1/(MK_q T_I)$, $c_{21} = c_{11}(0.25 - x_{ac})$, $c_{22} = c_{12}(0.25 - x_{ac})$, $c_{25} = A_3/(MK_{\alpha M} T_I b_3)$, $c_{26} = A4/(MK_{\alpha M} T_I b_4)$, $c_{27} = -0.0625 C_{n\alpha}\beta^2 b_5 V/b$, and $c_{28} = 7/(12MK_{qM} T_I)$, in which $C_{n\alpha}$ = $2\pi/\beta$ rad^{-1} is the curve slope of normal force versus angle of attack.

The first of the four nonlinear state variables $(x_9,\ \ldots,\ x_{12})$ is related to the leading edge stall and involves steady and unsteady contributions. Under unsteady conditions, a phase lag will manifest in the value of C_n (redefined as $C_n^{'}$) due to changes in the angle of attack over time, such that,

$$\dot{x}_9 = \frac{V\,(C_n^p - x_9)}{bT_p} \quad \text{and} \quad x_9 = C_n^{'}, \tag{7}$$

where T_p is a time constant associated with the phase lag, that depends on the leading edge pressure (according to the airfoil profile and Mach Number). Flow separation takes place while $|C_n^{'}| \geq C_{n_1}$ (otherwise, the flow is attached), where C_{n_1} is the value of C_n in the vicinity of static stall. A cumulative counter,

$$\tau_{\nu_{(k+1)}} = \tau_{\nu_{(k)}} + Vt/b, \tag{8}$$

is defined to quantify the dimensionless time elapsed when a vortex travels lengthwise from the separation point up to the trailing edge (k is a dummy discrete time counter variable).

To introduce the phase lag effects under unsteady conditions, an equivalent angle of attack is defined,

$$\alpha_F = \frac{x_9}{C_{n_\alpha}} = \frac{C_n^{'}}{C_{n_\alpha}}, \tag{9}$$

which represents the static angle value that would result in the same pressure at the leading edge of the airfoil in an hypothetical case with the phase lag neglected.

The nonlinear states x_{10} and x_{11} are based on the classical Kirchhoff theory for two-dimensional flow around a flat plate, as depicted in Fig. 2, and introduce the effects of flow separation and vortex shedding at the trailing edge of the airfoil. The point of flow separation, f (normalized by the chord length), is predicted in terms of the angle of attack,

$$f = \begin{cases} 1 - 0.3\exp\left[\left(|\hat{\alpha}| - \alpha_1\right)/s_1\right] & \text{if } |\hat{\alpha}| \leq \alpha_1 \\ 0.04 - 0.66\exp\left[\left(\alpha_1 - |\hat{\alpha}|\right)/s_2\right] & \text{otherwise} \end{cases}, \tag{10}$$

where α_1 is the static stall angle (typically obtained when $f = 0.7$), S_1 and S_2 are empirically determined stall parameters, and $\hat{\alpha}$ is an instantaneous value of angle of attack (in which $\hat{\alpha}$ = α or $f(C_n'/C_{n\alpha})$, depending on the case). Moreover,

$$\dot{C}_v = \begin{cases} C_n^c\left[1 - 0.25\left(1 + \sqrt{f''}\right)^2\right] & \text{if } \tau_v \leq 2T_{vl} \\ 0 & \text{otherwise} \end{cases}. \tag{11}$$

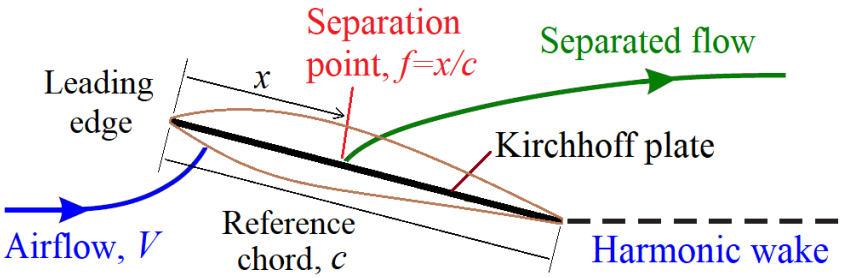

Figure 2. Definition of the chord-wise point of two-dimensional flow separation on a flat plate at angle of attack.

The second nonlinear state is defined,

$$\dot{x}_{10} = \frac{V\left(f - x_{10}\right)}{bT_f} \quad \text{and} \quad x_{10} = f^{''}, \tag{12}$$

where $f^{''}$ is the flow-separation point when phase lag is accounted for. The time parameter T_f is related to the flow state with respect to the vortex shedding phase (*i.e.*, before, during, or after, the vortex shedding). During the vortex shedding phase,

$$T_f = \begin{cases} T_{f0} & \text{if } \quad 0 \leq \tau_\nu \leq T_{\nu l} \quad \text{and} \quad \alpha\dot{\alpha} \geq 0 \\ 0.33T_{f0} & \text{if } \quad T_{\nu l} < \tau_\nu \leq 2T_{\nu l} \quad \text{and} \quad \alpha\dot{\alpha} \geq 0 \\ 0.33T_{f0} & \text{if } \quad 0 \leq \tau_\nu \leq 2T_{\nu l} \quad \text{and} \quad \alpha\dot{\alpha} < 0 \\ 4T_{f0} & \text{if } \quad 2T_{\nu l} < \tau_\nu \end{cases}, \tag{13}$$

where T_{f0} and $T_{\nu l}$ are empirical parameters. During this phase, the α_1 angle parameter is affected by an amount indicated by δ_{α_1}, such that,

$$\alpha_1 = \begin{cases} \alpha_{1_0} & \text{if } \quad \alpha\dot{\alpha} \geq 0 \\ \alpha_{1_0} - (1 - x_{10})^{0.25}\delta_{\alpha_1} & \text{otherwise} \end{cases}. \tag{14}$$

After the vortex shedding phase (when $|C_n^{'}| < C_{n_1}$) the time and angle parameters above are redefined,

$$T_f = \begin{cases} T_{f0} & \text{if } \quad f^{''} \geq 0.7 \\ 2T_{f0} & \text{otherwise} \end{cases} \quad \text{and} \quad \alpha_1 = \alpha_{1_0}. \tag{15}$$

The third nonlinear aerodynamic state represents the significant pitching moments created by displacements in the airfoil center of pressure due to the vortex shedding,

$$\dot{x}_{11} = \frac{2V\left(f - x_{11}\right)}{bT_{f_0}} \quad \text{and} \quad x_{11} = f_m. \tag{16}$$

With the relations above, contributions to the aerodynamic loading may be defined,

$$C_n^f = C_n^c \left(\frac{1+\sqrt{f''}}{2} \right)^2 , \tag{17}$$

$$C_m^f = C_n^c \left\{ K_0 + K_1(1-\hat{f}) + K_2 \sin(\pi \hat{f}^m) \right\} + C_{M_0}, \tag{18}$$

$$C_t^f = \eta C_{n_\alpha} \sqrt{f''} {\alpha_E}^2, \tag{19}$$

where $C_n^c = C_{n_\alpha} \alpha_E$ is the normal contribution of the circulatory aerodynamic portion, in which,

$$\alpha_E = \beta^2 \frac{V}{b} \left(A_1 b_1 x_1 + A_2 b_2 x_2 \right), \tag{20}$$

is the effective angle of attack, m has a typical value of 2, K_0, K_1, and K_2 are empirical parameters related to the pitching moment under static conditions, C_{M_0} is the zero-lift pitching moment coefficient, η is a fraction of the tangential force experienced by the airfoil when compared with an hypothetical value predicted by the potential flow theory, and $\hat{f} = \max[x_{10}, x_{11}]$.

The fourth nonlinear state is associated with the evolution of the dynamic stall phenomenon, and accounts for the effects of vortex shed at the leading edge of the airfoil, travel along the airfoil body, and egress at the trailing edge. This state is defined,

$$\dot{x}_{12} = \frac{V\left(\dot{C}_\nu - x_{12}\right)}{bT_\nu} \quad \text{and} \quad x_{12} = C_n^\nu, \tag{21}$$

and, as before, $C_n^{'}$ is assumed as a reference value. Vortices will be discarded while the critical value is not achieved (*i.e.*, before the onset of the vortex shedding phase). As the critical value is reached and the vortex shedding phase takes place, the dimensionless time counter (τ_ν) is used to track the vortex traveling along the airfoil, such that,

$$T_\nu = \begin{cases} T_{\nu_0} & \text{if} \quad 0 \le \tau_\nu \le T_{\nu l} \quad \text{and} \quad \alpha\dot{\alpha} \ge 0 \\ 0.25T_{\nu_0} & \text{if} \quad T_{\nu l} < \tau_\nu \le 2T_{\nu l} \quad \text{and} \quad \alpha\dot{\alpha} \ge 0 \\ 0.5T_{\nu_0} & \text{if} \quad 0 \le \tau_\nu \le 2T_{\nu l} \quad \text{and} \quad \alpha\dot{\alpha} < 0 \\ 0.9T_{\nu_0} & \text{if} \quad 2T_{\nu l} < \tau_\nu \end{cases} . \tag{22}$$

The normal force coefficient related to the vortex shedding may be defined,

$$C_\nu = \begin{cases} C_n^c \left[1 - 0.25 \left(1 + \sqrt{f''} \right)^2 \right] & \text{if} \quad \tau_\nu \le 2T_{\nu l} \\ 0 \quad \text{otherwise} \end{cases} . \tag{23}$$

An expression for the pitching moment coefficient, which accounts for the change in the center of pressure location as the vortex travels along the airfoil body, is also defined,

$$C_m^\nu = -0.25 \left[1 - \cos\left(\frac{\pi \tau_\nu}{T_{\nu l}} \right) \right] C_n^\nu. \tag{24}$$

By considering all contributions, the pitching moment and lifting force coefficients are defined,

$$C_{m_{\text{ec}}} = C_m^p + C_m^f + C_m^\nu + \left(C_n^p - C_n^c + C_n^f + C_n^\nu \right) \left(x_{\text{ec}} - x_{\text{ac}} \right), \tag{25}$$

$$C_l = \left(C_n^p - C_n^c + C_n^f + C_n^\nu \right) \cos\alpha - C_t^f \sin\alpha. \tag{26}$$

3. Pitch-and-Plunge-Airfoil Model

The coupled equations of motion of a 2-DoF PAPA model are presented in the well-known dimensionless form, with damping and aerodynamic loading included,

$$\begin{bmatrix} 1 & 0 & 0 & 0 \\ 0 & \mu_e & 0 & x_\theta \\ 0 & 0 & 1 & 0 \\ 0 & x_\theta & 0 & r_\theta^2 \end{bmatrix} \begin{bmatrix} \dot{\bar{h}} \\ \ddot{\bar{h}} \\ \dot{\theta} \\ \ddot{\theta} \end{bmatrix} = \begin{bmatrix} 0 & 1 & 0 & 0 \\ -\omega_h^2 & -\zeta_{hh} & 0 & -\zeta_{h\theta} \\ 0 & 0 & 0 & 1 \\ 0 & -\zeta_{\theta h} & -r_\theta^2 \omega_\theta^2 & -\zeta_{\theta\theta} \end{bmatrix} \begin{bmatrix} \bar{h} \\ \dot{\bar{h}} \\ \theta \\ \dot{\theta} \end{bmatrix} + \frac{V^2}{\mu\pi b^2} \begin{bmatrix} 0 & 0 \\ -1 & 0 \\ 0 & 0 \\ 0 & 2 \end{bmatrix} \begin{bmatrix} C_l \\ C_{m_{\text{ec}}} \end{bmatrix}, \tag{27}$$

where $\bar{h} = h/b$ is the plunge displacement in semichords, μ_e is the plunge-to-pitch mass ratio, r_θ is the radius of gyration, $\omega_{()}$ are frequency-related parameters, $\zeta_{()()}$ are damping parameters, and μ is the air mass ratio.

4. RESULTS

This section describes the model parameters, a model verification against literature data, and original study cases. A traditional Runge-Kutta method is used to solve the model equations. Effort is made to depict the more expressive changes in the predicted aeroelastic behavior of the airfoil model when linear and nonlinear aerodynamic models are considered. Later, the effects of SMA springs are considered along with nonlinear aerodynamics to reveal attractive post-flutter scenarios with bounded oscillations at above the linear critical flutter speed.

4.1 Model Parameters

Two sets of airfoil parameters are considered in this work. First, the parameters of Santos *et al.* (2017) are assumed for verification purposes, c = 0.25 m, x_{ec} = 0.25, x_{ac} = 0.25, m_θ = 1.50 kg, m_h = 3.67 kg, x_θ = 0.66, r_θ = 0.73, ζ_{hh} = 5.49, ζ_{ah} = 10.03, ζ_{ha} = 10.03, ζ_{aa} = 32.48, ω_h = 34.07 rad·s^{-1}, ω_θ = 24.85 rad·s^{-1}. Then the parameters of Sousa and De Marqui Junior (2016) are assumed to investigate the cases with SMA springs (so that previously reported results may be appreciated for different aerodynamic models), c = 0.25 m, x_{ec} = 0.25, x_{ac} = 0.25, m_θ = 1.54 kg, m_h = 4.09 kg, x_θ = 0.256, r_θ = 0.547, ζ_{hh} = 9.48, ζ_{ah} = 4.34, ζ_{ha} = 4.34, ζ_{aa} = 2.32, ω_h = 52.19 rad·s^{-1}, ω_θ = 26.56 rad·s^{-1}. In all cases of this work the Beddoes-Leishman aerodynamic parameters of Santos *et al.* (2017) are assumed, T_I = 0.00072886 s, T_p = 1.7, α_{1_0} = 15.25º, δ_{α_1} = 2.1º, T_{f_0} = 3, T_{vl} = 7, T_{v_0} = 6, K_0 = 0.0025, K_1 = −0.135, K_2 = 0.04, η = 0.965, m = 2, C_{m_0} = 0, and C_{n_1} = 1.45. The assumed speed of sound is V_s = 343 m·s^{-1}.

The SMA phase transformation parameters and spring geometry are the same of Sousa and De Marqui Junior (2016), most of them omitted here for brevity, but it is suffice to mention that the SMA elements operate in the pseudoelastic regime (above the austenite finish temperature, *i.e.*, with $T_\infty \geq A_f$) and that the airfoil is designed to exhibit the same elastic restoring moment of a reference configuration when no SMA phase transformation takes place (so that the linear flutter speed is the same in both cases). A detailed discussion on the effects of preloaded SMAs is presented in Sousa and De Marqui Junior (2016) and experimentally demonstrated in Sousa and De Marqui (2018) and Sousa *et al.* (2017). The applied preload is fundamental to allow the SMA stress-induced phase transformation to occur (hence, the hysteretic damping to manifest) at relatively small aeroelastic displacements and of particular importance at post-flutter regime to transform unstable divergent oscillations into persistent, bounded oscillations. The appropriate amount of preload, however, is particular for specific model characteristics and the application of excessive preload could, for example, provoke loading-unloading cycles displaced in the stress-strain plane in such a way the critical stresses for SMA austenitic recovery is never reached and, therefore, no hysteretic damping takes place.

4.2 Preliminary Aerodynamic Model Verification

First (before the inclusion of SMAs in the aeroelastic model), the nonlinear Beddoes-Leishman aerodynamic model implemented in this work was verified against literature data from Santos *et al.* (2017). The results of the referred article were satisfactorily reproduced, with minor differences in the predicted critical flutter speed and in the amplitudes of oscillation. The flutter speed predicted by the model implemented in this work (for the parameters in Santos *et al.* (2017)) is 14.5 m·s^{-1}, while the reported experimental value is 14.2 m·s^{-1} (and reported predicted value of 13.7 m·s^{-1}). This verification is briefly depicted in Fig. 3 at flutter and post-flutter conditions with linear and nonlinear aerodynamics. At the flutter boundary the oscillations are marginally stable and tend to follow the applied initial disturbance. At post-flutter regime the oscillations exhibit linear dynamically unstable behavior over time while nonlinear effects are not achieved and turn into limit-cycles of finite amplitudes when nonlinear effects take place. The predicted nonlinear behavior for the linear model is not related to aerodynamic effects and may be attributed only to numerical issues at unacceptably large displacements. The nonlinear behavior obtained by the full Beddoes-Leishman model, in turn, is related to nonlinear aerodynamic phenomena and is in agreement with the literature, as discussed, for example, in Santos *et al.* (2017).

4.3 Flutter-Boundary Cases with SMAs and Nonlinear Aerodynamics

The results of Sousa and De Marqui Junior (2016) (for an airfoil with SMA springs) are revisited here when the Beddoes-Leishman model is considered. The referred work originally considers the linear Jones' exponential approximation in state-space form (Edwards *et al.*, 1979) to represent the unsteady aerodynamic loading, which is unable to capture stall-related effects. The critical speed predicted here (about 11.7 m·s^{-1}) is in agreement with the referred work regardless of the different aerodynamic model, as expected. If no preload is considered applied to the SMA springs no stress-induced phase transformation takes place and the airfoil behaves as in a conventional configuration with linear torsional spring, as shown in Fig. 4(a) for the critical airflow speed (with arbitrary initial condition of $\bar{h}(0) = 0.08$). For the same conditions and 3 N of preload, the added damping of SMA hysteresis decreases the amplitudes of oscillation, as shown in Fig. 4(b), also in agreement with Sousa and De Marqui Junior (2016). The responses are comparable for both linear and nonlinear aerodynamics as expected, since no significant stall-related effects manifest at relatively small airfoil motions.

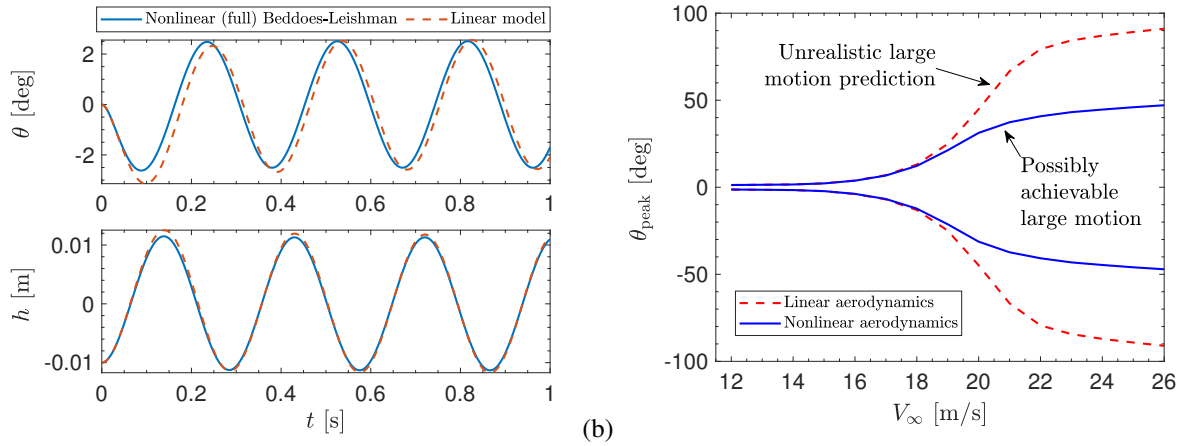

(a) (b)

Figure 3. Beddoes-Leishman model verification against literature data (*cf.* Santos *et al.* (2017) for details and experimental data). (a) Pitch and plunge motions at flutter condition. (b) Post-flutter pitch response (peak values) for a wide range of airflow speeds with linear and nonlinear aerodynamics.

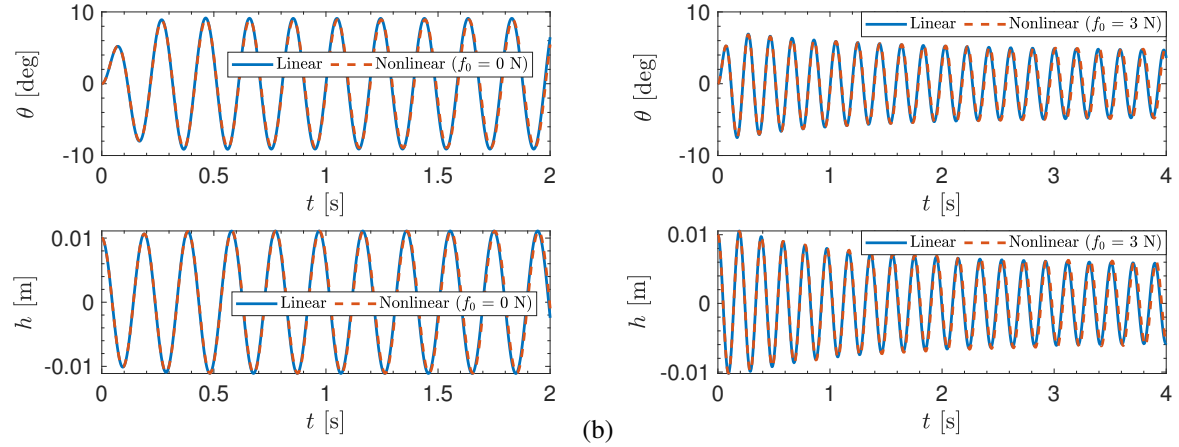

(a) (b)

Figure 4. (a) Pitch and plunge responses considering linear and nonlinear aerodynamics at flutter condition with linear torsional stiffness (without SMA phase transformation). (b) Responses for the same aerodynamic conditions with preloaded SMA springs (with stress-induced SMA phase transformation).

4.4 Post-Flutter Cases with SMAs and Nonlinear Aerodynamics

In post-flutter condition, as shown in Fig. 5 for the (arbitrary) airflow speed of 13 m·s^{-1}, the aeroelastic displacements become massively large over time. With linear aerodynamics the predicted amplitudes of oscillation reach improbable values. With nonlinear aerodynamics bounded oscillations are predicted at more reasonable amplitudes and, although notably large, they may be physically achievable as experimentally demonstrated during wind-tunnel tests in Santos *et al.* (2017). Moreover, in production wind turbine generators the resulting relative wind may eventually occur in orientations such that the (aerodynamic) angle of attack is significantly large even though the (geometric) incidence angle remains small. Therefore, stall-related dynamic phenomena may take place at large aerodynamic angles of attack and small structural angles of incidence, particularly important in this study since the SMA springs are associated solely with the angular pitch motion (structural angle varying over time), although a fixed component of wind speed is assumed here and any variations in airflow characteristics are only related to the airfoil motion.

The post-flutter behavior for preloaded SMA springs is expressively modified with respect to a structurally linear reference configuration, and the degree of applied preload should be appreciated carefully (Sousa and De Marqui Junior, 2016; Sousa and De Marqui, 2018). A case without preload, $f_0 = 0$ N, is also shown for comparison, with negligible SMA effects. For discussion purposes, a specific value of preload is considered ($f_0 = 3$ N), and a relatively modest post-flutter regime is predicted, but it is enough to depict changes in the airfoil behavior for linear and nonlinear aerodynamic models. Figure 6 shows post-flutter responses over time for 13 m·s^{-1} and SMA springs when nonlinear aerodynamics is considered (for the same preload and linear aerodynamics, the response would become large at 12.5 m·s^{-1}). Stress-induced SMA phase transformation is achieved at small displacements so that the effects of hysteretic damping are pronounced. Similar results are predicted for 15 m·s^{-1}, but such speed could not be achieved for linear aerodynamics even with higher preload.

Figure 7 shows the pitch and plunge displacements predicted at 15 m·s^{-1} with preloaded SMA springs for linear and

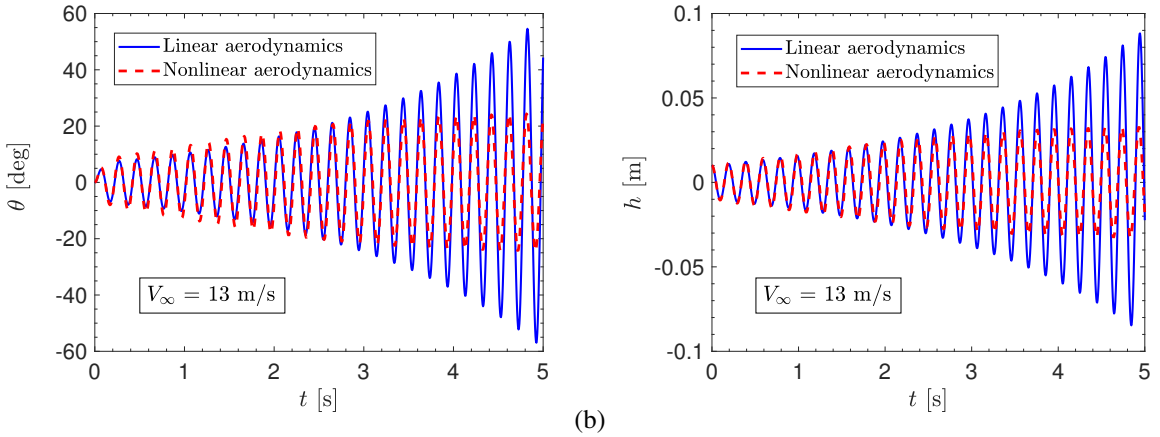

Figure 5. Pitch (a) and plunge (b) post-flutter responses at 13 m·s^{-1} for linear and nonlinear aerodynamics. Linear torsional stiffness is assumed in both cases (without SMA phase transformation).

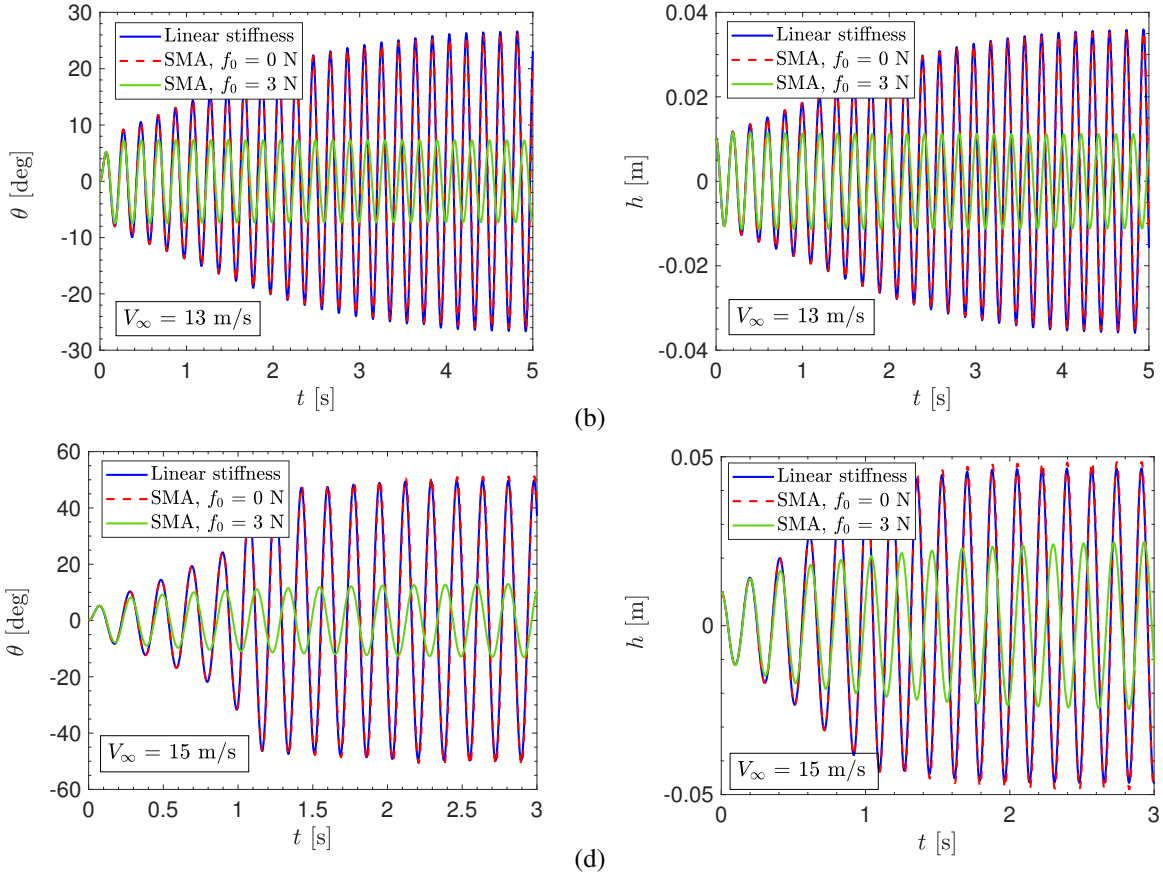

Figure 6. Pitch and plunge displacements over time at 13 m·s^{-1} (a, b) and 15 m·s^{-1} (c, d) for nonlinear aerodynamics and SMA springs (with stress-induced phase transformation).

nonlinear aerodynamics. While a wider range of post-flutter regime is predicted, the amplitudes of oscillation increase significantly for both aerodynamic models. With nonlinear aerodynamics, however, smaller amplitudes are predicted for the same airflow speed since stall-related effects tend to depreciate lift generation. In this sense, it is possible to achieve higher airflow speeds when combined nonlinear effects take place, revealing attractive post-flutter scenarios. While both nonlinear contributions transform unstable oscillations into stable ones, the results suggest that aerodynamic effects are convenient to promote stable oscillations at airflow speeds higher than those obtained for the isolated SMA case, while the SMA pseudoelastic hysteretic damping is effective to reduce the amplitudes of oscillations at a certain airflow speed when an appropriate degree of preload is considered. Therefore, it is predicted that the combined nonlinear effects are more attractive than the isolated effects to promote stable post-flutter oscillations, what is also attractive to airfoil-based energy harvesting cases since relatively wider ranges of airflow speeds may be exploited for persistent conversion of vibration

energy into usable electrical energy while maintaining acceptable motions.

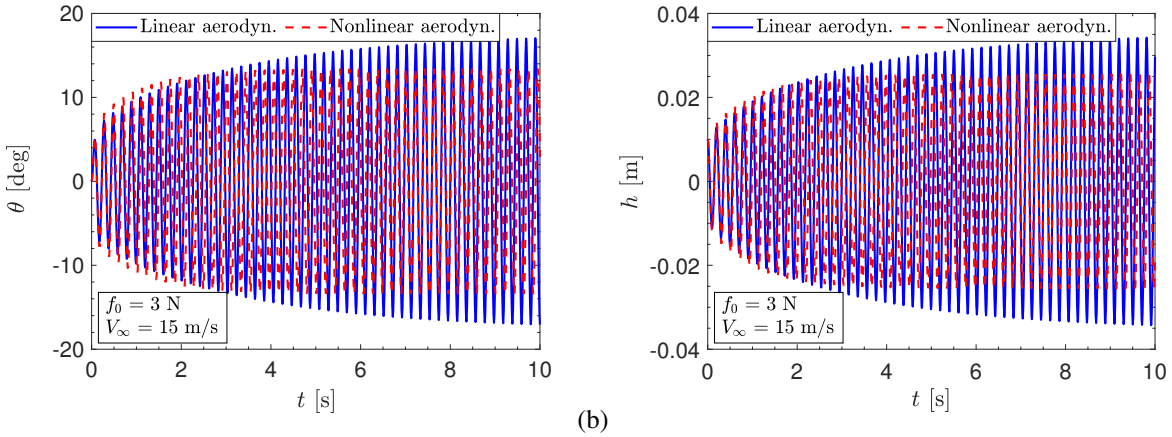

Figure 7. Pitch (a) and plunge (b) displacements over time at 15 m·s^{-1} for linear and nonlinear aerodynamics and preloaded SMA springs.

The results (in particular in Fig. 7) are attractive in the context of (fluttering) airfoil-based energy harvesting since more reasonable amplitudes of oscillations are predicted at larger post-flutter airflow speeds. In Sousa and De Marqui Junior (2015), for example, the linear aerodynamic model of Edwards *et al.* (1979) is employed and the range of post-flutter airflow speeds is intentionally limited accordingly to the achieved amplitudes of oscillation to maintain a certain degree of reliability of the predicted aeroelastic response. In an eventual experimental verification the upper limit of post-flutter airflow speeds would be constrained to provide experimental data consistently comparable with (linear) simulation results. With nonlinear aerodynamics this restriction may be eliminated since the highly nonlinear aerodynamic loading associated with larger displacements can be satisfactorily represented by the numerical model, and any further limitation would be imposed by other structural restrictions. Therefore, further studies with the nonlinear model may be conducted, for example, to investigate more attractive configurations to either wind turbine blade sections or intentionally stalled aerodynamic surfaces for airfoil-based (piezoelectric or electromagnetic) aeroelastic energy harvesters.

5. CONCLUSIONS

A traditional pitch-and-plunge-airfoil (PAPA) model is considered in this study to investigate the aeroelastic behavior of the airfoil in the presence of combined structural and aerodynamic nonlinearity sources. The structural nonlinear behavior is introduced via the hysteresis of shape-memory alloy (SMA) springs operating in the pseudoelastic regime. The aerodynamic nonlinear behavior is introduced via the representation of stall-related effects provided by the Beddoes-Leishman model. Numerical results reveal expressive differences in the predictions when linear and nonlinear aerodynamic models are considered (in agreement with experimental data from the literature). Attractive post-flutter scenarios are predicted when combined structural and aerodynamic nonlinearities are considered. Bounded oscillations are predicted for airflow speeds significantly higher than the linear critical flutter speed of the airfoil model due to the combined structural and aerodynamic nonlinear effects. While both nonlinear contributions transform unstable oscillations into stable ones, the numerical predictions suggest that aerodynamic stall effects are more effective in the sense of promoting stable oscillations at higher airflow speeds (when compared with the purely structurally nonlinear case), while the SMA pseudoelastic hysteretic damping is more effective to reduce the amplitudes of oscillations. The combined effects, however, seem more attractive than the individual effects to promote stable post-flutter scenarios, what is attractive to airfoil-based energy harvesting cases and also to wind turbine applications.

6. ACKNOWLEDGEMENTS

This work has been developed within the scopes of the "*Study of the dynamic stall on wind-turbine blade section under non-linear aeroelastic behavior*" research project funded by the National Council for Scientific and Technological Development (CNPq/Brazil, grant number 423369/2021-0, coordinated by Prof. Dr. Daniel Sampaio Souza) and the CNPq–Research Group in Structures, Manufacturing and Materials (GPEM2, coordinated by Prof. Dr. Crystopher Cardoso de Brito). The available infrastructure and experimental apparatus provided by the Laboratory of Aeronautics of the School of Engineering of Sao Joao da Boa Vista (FESJ–Unesp) and by the FINEP Project "Cutting Edge Research in New UNESP Campus: Telecommunications, Aeronautical, Optoavionics" (grant number 0527/18) are greatly appreciated. The authors declare no perceived conflict of interest.

7. REFERENCES

Beddoes, T.S., 1978. "Onset of leading edge separation effects under dynamic conditions and low mach number".

Bisplinghoff, R.L., Ashley, H. and Halfman, R.L., 1955. *Aeroelasticity*. Addison-Wesley Publishing Company, Inc., Cambridge, Massachussets.

Brinson, L.C., 1993. "One-Dimensional Constitutive Behavior of Shape Memory Alloys: Thermomechanical Derivation with Non-Constant Material Functions and Redefined Martensite Internal Variable". *Journal of Intelligent Material Systems and Structures*, Vol. 4, No. 2, pp. 229–242. ISSN 1045-389X. doi:10.1177/1045389X9300400213. URL http://jim.sagepub.com/cgi/doi/10.1177/1045389X9300400213.

Dowell, E.H., 2015. *A Modern Course in Aeroelasticity*, Vol. 217 of *Solid Mechanics and Its Applications*. Springer International Publishing, Cham, 5th edition. ISBN 978-3-319-09452-6. doi:10.1007/978-3-319-09453-3. URL http://link.springer.com/10.1007/978-3-319-09453-3.

Edwards, J.W., Ashley, H. and Breakwell, J.V., 1979. "Unsteady aerodynamic modeling for arbitrary motions". *AIAA Journal*, Vol. 17, No. 4, pp. 365–374. doi:10.2514/3.7348. URL http://arc.aiaa.org/doi/abs/10.2514/3.7348.

Lee, B.H.K., Price, S.J. and Wong, Y.S., 1999. "Nonlinear aeroelastic analysis of airfoils: bifurcation and chaos". In *Progress in Aerospace Sciences*. Elsevier Science Ltd., Vol. 35, pp. 205–334. doi:10.1016/S0376-0421(98)00015-3. URL sciencedirect.com/science/article/pii/S0376042198000153.

Leishman, J.G. and Beddoes, T.S., 1986. "A generalized model for airfoil unsteady aerodynamic behavior and dynamic stall using indicial method".

Leishman, J.G. and Beddoes, T.S., 1989. "A semi-empirical model for dynamic stall". *Journal of the American Helicopter Society*, Vol. 34, pp. 3–17.

Leishman, J.G. and Crouse, G.L., 1989a. "A state-space model of unsteady aerodynamics in a compressible flow for flutter analyses". *Aerospace Sciences Meeting*. doi:10.2514/6.1989-22.

Leishman, J.G. and Crouse, G.L., 1989b. "State-space models for unsteady airfoil behavior and dynamic stall". AIAA 89-1319, pp. 1372–1383.

Santos, C.R.d., Marques, F.D. and Hajj, M.R., 2019. "The effects of structural and aerodynamic nonlinearities on the energy harvesting from airfoil stall-induced oscillations". *Journal of Vibration and Control*, Vol. 25, No. 14, pp. 1991–2007. ISSN 1077-5463. doi:10.1177/1077546319844383. URL https://journals.sagepub.com/doi/10.1177/1077546319844383.

Santos, C.R.d., Pereira, D.A. and Marques, F.D., 2017. "On limit cycle oscillations of typical aeroelastic section with different preset angles of incidence at low airspeeds". *Journal of Fluids and Structures*, Vol. 74, pp. 19–34. ISSN 0889-9746. doi:10.1016/j.jfluidstructs.2017.07.008. URL https://www.sciencedirect.com/science/article/pii/S0889974617302396.

Sousa, V.C. and De Marqui, C., 2018. "Experimental study on the aeroelastic behavior of a typical airfoil section with superelastic shape memory alloy springs". *Journal of Intelligent Material Systems and Structures*, Vol. 29, No. 4, pp. 623–635. ISSN 1045-389X. doi:10.1177/1045389X17721024. URL https://doi.org/10.1177/1045389X17721024.

Sousa, V.C. and De Marqui Junior, C., 2015. "Airfoil-based piezoelectric energy harvesting by exploiting the pseudoelastic hysteresis of shape memory alloy springs". *Smart Materials and Structures*, Vol. 24, No. 12, p. 125014. ISSN 0964-1726. doi:10.1088/0964-1726/24/12/125014. URL https://doi.org/10.1088/0964-1726/24/12/125014.

Sousa, V.C. and De Marqui Junior, C., 2016. "Effect of pseudoelastic hysteresis of shape memory alloy springs on the aeroelastic behavior of a typical airfoil section". *Journal of Intelligent Material Systems and Structures*, Vol. 27, No. 1, pp. 117–133. ISSN 1045-389X. doi:10.1177/1045389X14563862. URL https://doi.org/10.1177/1045389X14563862.

Sousa, V.C., De Marqui Junior, C. and Elahinia, M., 2017. "Aeroelastic behavior of a typical section with shape memory alloy springs: Modeling nonhomogeneous distribution of state variables". *Applied Mathematical Modelling*, Vol. 52, pp. 404–416. ISSN 0307904X. doi:10.1016/j.apm.2017.07.056. URL https://doi.org/10.1016/j.apm.2017.07.056.

Vasconcellos, R.M.G., Pereira, D.A. and Marques, F.D., 2016. "Characterization of nonlinear behavior of an airfoil under stall-induced pitching oscillations". *Journal of Sound and Vibration*, Vol. 372, pp. 283–298. ISSN 0022-460X. doi:10.1016/j.jsv.2016.02.046. URL https://www.sciencedirect.com/science/article/pii/S0022460X16002066.

8. RESPONSIBILITY NOTICE

The authors are solely responsible for the printed material included in this paper.